Mechanics Research Communications 42 (2012) 60–67

Contents lists available at SciVerse ScienceDirect

Mechanics Research Communications

journal homepage: www.elsevier.com/locate/mechrescom

Adaptive reorientation of cardiac myofibers: The long-term effect of initial and boundary conditions

M. Pluijmert[a,*], W. Kroon[a], T. Delhaas[a], P.H.M. Bovendeerd[b]

[a] Department of Biomedical Engineering, Cardiovascular Research Institute Maastricht, Maastricht University, P.O. Box 616, NL-6200 MD Maastricht, The Netherlands
[b] Department of Biomedical Engineering, Eindhoven University of Technology, P.O. Box 513, NL-5600 MB Eindhoven, The Netherlands

ARTICLE INFO

Article history:
Received 29 July 2011
Received in revised form 1 November 2011
Available online 2 December 2011

Keywords:
Myocardial structure
Finite-element model
Cardiac mechanics
Cardiac deformation

ABSTRACT

On the basis of results from modeling and experimental studies it has been hypothesized that myocytes adapt their orientation to achieve a preferred mechanical load. In a previous computational model study in which fiber reorientation was considered as a local response to local fiber cross-fiber shear strain, we have shown that predicted left ventricular (LV) myofiber orientations agreed well with experimental data. In this study, we investigated in the latter model the effect of initial and boundary conditions on predicted fiber orientations on the long term. After adaptation, predicted fiber orientation and deformation became more realistic, irrespective of initial and boundary conditions. As adaptation proceeded, the effect of initial conditions was found to disappear, suggesting that one single optimal fiber orientation field exists for the heart. In contrast, the effect of the boundary conditions persisted, indicating that modeling of in particular the interaction between myocardium and valvular annulus is relevant for predicting LV myofiber reorientation.

1. Introduction

Several finite element (FE) models have been developed that are capable of describing the forward relation between cardiac tissue properties and clinically assessable parameters of pump (dys)function (Bovendeerd et al., 2009; Costa et al., 2001; Kerckhoffs et al., 2003). Gradually, attempts are made to enhance clinically obtained diagnostic information by employing these computational models in an inverse mode (Hunter et al., 2010). In addition, the models might be used to assist in treatment selection by simulating the acute effect of candidate interventions beforehand. As interventions may cause cardiac adaptation on the long term, the current models should be extended with a description of the adaptive properties of the myocardium.

Previous model studies have shown that strain distribution in the cardiac wall is highly dependent on myofiber orientation (Bovendeerd et al., 2009; Ubbink et al., 2006). In experimental studies a change in myofiber orientation was observed when mechanical properties of the surrounding tissue were altered (Weis et al., 2000; Zimmerman et al., 2000). In addition, myofiber strain exhibits little regional heterogeneity during ejection throughout the LV wall (Delhaas et al., 1993; Waldman et al., 1988). From these observations it was hypothesized that myocytes might adapt orientation to achieve a preferred mechanical load (Arts et al., 1994).

According to the hypothesis of myofiber reorientation, Rijcken et al. (1999) performed a model study where a parameterized distribution of fiber orientations was optimized for minimal heterogeneity in myofiber shortening during ejection. At minimum heterogeneity, fiber orientations were found to compare favorably with experimental data. While it was shown that myofiber orientations can be predicted on the basis of a simple criterion, a global parameterized distribution is not apt to predict local reorientation of myofibers during, e.g., disease. Kroon et al. (2009a) developed a non-parameterized model in which fiber reorientation was considered as a local response to local fiber cross-fiber shear strain. Their model was also capable of predicting a realistic LV structure. During the adaptation process a significant increase in homogenization of mechanical load over the LV wall was obtained and the LV generated more pump work with the same amount of mass.

The aim of this study is to further investigate the computational model by Kroon et al. (2009a), in particular with respect to the effect of initial fiber orientations and the influence of boundary conditions at the base on long-term outcome of the adaptive process.

2. Methods

2.1. Modeling myofiber reorientation

Kroon et al. (2009a) modeled myofiber reorientation as a response to local loss of myocardial integrity due to forces generated by fiber cross-fiber shear strains during myofiber contraction. These shear forces affect connections between extra-cellular

* Corresponding author. Tel.: +31 433881659.
E-mail address: marieke.pluijmert@maastrichtuniversity.nl (M. Pluijmert).

0093-6413/$ – see front matter © 2011 Elsevier Ltd. All rights reserved.
doi:10.1016/j.mechrescom.2011.11.011

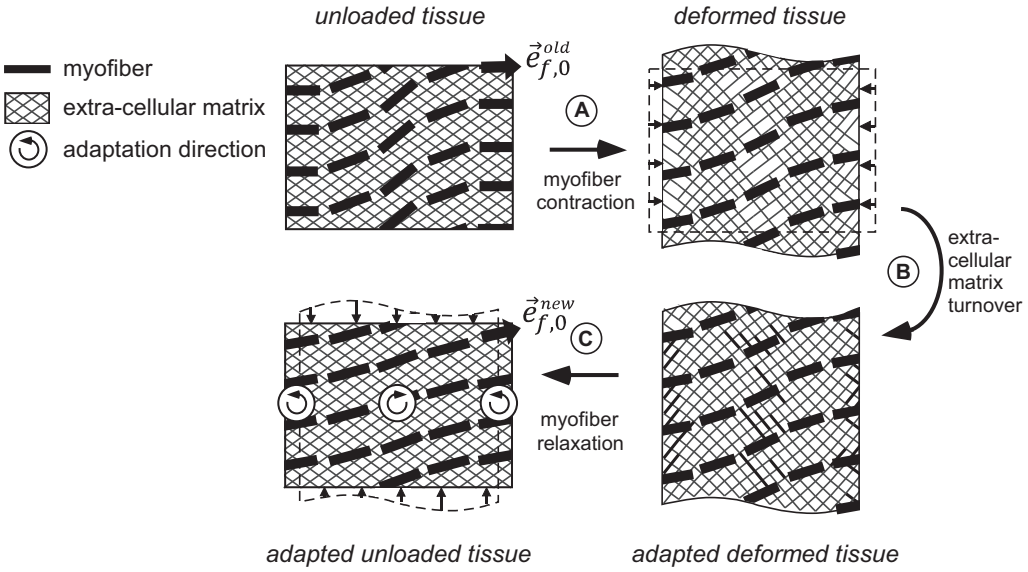

Fig. 1. Schematic description of the hypothesis on adaptation of myofiber orientation where the old unloaded myofiber direction $\vec{e}_{f,0}^{\text{old}}$ evolves through A, B, and C towards the new adapted unloaded myofiber direction $\vec{e}_{f,0}^{\text{new}}$ (Kroon et al., 2009a).

matrix (ECM) and myofibers (Fig. 1). New connections are continuously formed during diastolic and systolic phase of the cardiac cycle. When a certain connection is made, the actual orientation field tends to be fixed within the tissue. The process of breaking and forming of ECM connections itself was not explicitly modeled. Instead, the evolution of the myofiber orientation in the unloaded state $\vec{e}_{f,0}$ towards the actual myofiber orientation $\vec{e}_f$ corrected for rigid body rotation was phenomenologically described by (Kroon et al., 2009a):

$$\frac{\partial \vec{e}_{f,0}}{\partial t} = \frac{1}{\kappa}(\vec{e}_f^{\,*} - \vec{e}_{f,0}) \tag{1}$$

with κ the adaptation time constant and $\vec{e}_f^{\,*}$ the myofiber direction corrected for rigid body rotations described by:

$$\vec{e}_f^{\,*} = \frac{\boldsymbol{U}\cdot\vec{e}_{f,0}}{\lambda_f}; \quad \lambda_f = |\boldsymbol{U}\cdot\vec{e}_{f,0}| \tag{2}$$

Here, λ_f represents the myofiber stretch ratio and $\boldsymbol{U}$ the tensor that describes deformation of the tissue excluding rigid body rotations $\boldsymbol{R}$ according to:

$$\boldsymbol{U} = \boldsymbol{R}^{-1}\cdot\boldsymbol{F} \tag{3}$$

with $\boldsymbol{F}$ the deformation gradient tensor. Since rigid body rotations are unlikely to be sensed by the tissue, they are considered irrelevant to adaptation and therefore excluded in evolution Eq. (1).

Notice that according to Eqs. (1)–(3), myofiber reorientation only occurs in case neither of the principal strain directions (eigenvectors of $\boldsymbol{U}$) coincides with the unloaded fiber direction $\vec{e}_{f,0}$, i.e., in case of fiber cross-fiber shear. To which of the principal strain directions the fiber orientation ultimately aligns, is not prescribed but follows from the deformation field.

2.2. Modeling cardiac mechanics

Tissue deformations during the cardiac cycle are calculated with the finite element (FE) model of LV mechanics by Bovendeerd et al. (2009), that will only be described in brief.

2.2.1. Geometry and myofiber orientation

In the passive stress-free state, a thick-walled geometry is assumed (Fig. 2). The endocardial and epicardial surfaces are described by truncated ellipsoids. In this state, wall and cavity volumes equal 136 ml and 44 ml, respectively. The unloaded geometry remains unaltered during adaptation. Myofiber orientation $\vec{e}_{f,0}$ is prescribed with respect to the local cardiac coordinate system $\{\vec{e}_{l,0}, \vec{e}_{t,0}, \vec{e}_{c,0}\}$, where the subscript 0 refers to the unloaded state. The transmural direction $\vec{e}_{t,0}$ is defined as the outer normal to the cardiac surfaces. The longitudinal direction $\vec{e}_{l,0}$ is defined perpendicular to $\vec{e}_{t,0}$ from apex to base. To obtain a right handed coordinate system, the circumferential direction $\vec{e}_{c,0}$ is defined in clockwise direction when viewing the LV in apex-to-base direction. Myofiber orientations are described by two angles. The helix angle $\alpha_{h,0}$ is defined as the angle between $\vec{e}_{c,0}$ and the projection of $\vec{e}_{f,0}$ on the circumferential–longitudinal plane $(\vec{e}_{c,0}, \vec{e}_{l,0})$. The transverse angle $\alpha_{t,0}$ is defined as the angle between $\vec{e}_{c,0}$ and the projection of $\vec{e}_{f,0}$ on the circumferential–transmural plane $(\vec{e}_{c,0}, \vec{e}_{t,0})$ (Fig. 2A).

2.2.2. Material properties

Myocardial tissue Cauchy stress $\boldsymbol{\sigma}$ is composed of a passive component $\boldsymbol{\sigma}_p$ and an active component σ_a:

$$\boldsymbol{\sigma} = \boldsymbol{\sigma}_p + \sigma_a \vec{e}_f \vec{e}_f \tag{4}$$

Active stress σ_a is modeled through a series arrangement of a contractile and a series elastic element. The magnitude of σ_a depends on time t_a elapsed since activation, sarcomere length l_s, and sarcomere shortening velocity $-\partial l_s/\partial t$ (Kerckhoffs et al., 2003):

$$\sigma_a = f\left(t_a, l_s, -\frac{\partial l_s}{\partial t}\right) \tag{5}$$

Active stress development is initiated simultaneously across the LV wall with a cycle time of 800 ms. Passive material behavior is assumed nonlinearly elastic, transversely isotropic, and nearly incompressible.

2.2.3. Governing equations and boundary conditions

In the model, the equations of conservation of linear momentum are solved:

$$\vec{\nabla}\cdot\boldsymbol{\sigma} = \vec{0} \tag{6}$$

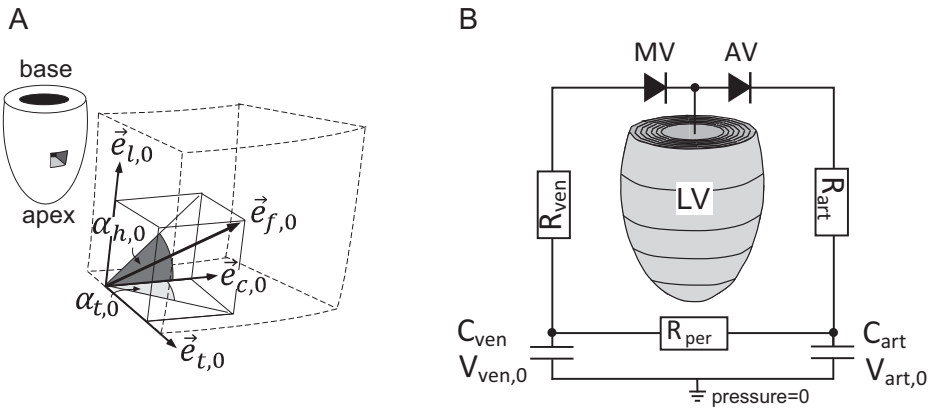

Fig. 2. Computational model of LV mechanics. (A) Ellipsoidally shaped model of LV mechanics showing myofiber orientation vector $\vec{e}_{f,0}$ described by $\alpha_{h,0}$ and $\alpha_{t,0}$ in a local cardiac coordinate system $\{\vec{e}_{l,0}, \vec{e}_{t,0}, \vec{e}_{c,0}\}$. (B) The finite element (FE) mesh consists of 30 elements and is incorporated in a lumped parameter model of the circulation. AV, aortic valve; C_{art}, arterial compliance; C_{ven}, venous compliance; MV, mitral valve; R_{art}, arterial resistance; R_{per}, peripheral resistance; R_{ven}, venous resistance; $V_{art,0}$, zero-pressure arterial volume; $V_{ven,0}$, zero-pressure venous volume.

with $\vec{\nabla}$ the spatial gradient operator. At the base, essential boundary conditions are defined to suppress rigid body motion and to represent the mechanical effect of structures left out of the model, e.g., the valvular annulus. The basal boundary conditions are subject of variation in this study (see Section 2.3). The epicardial surface is assumed to be traction free while the endocardial surface is uniformly subjected to left ventricular pressure p_{lv}. During isovolumic contraction (IC) and relaxation (IR) phases of the cardiac cycle, p_{lv} is determined such that mechanical equilibrium of the myocardial tissue is obtained at a constant end-diastolic or end-systolic left ventricular volume, respectively. During the filling and ejection phase, p_{lv} is computed from the interaction of the LV with the circulation as described in Bovendeerd et al. (2009).

2.2.4. Numerical implementation

The equilibrium equations (6) are solved numerically with a Galerkin type finite element method using 27-noded hexahedral elements with a tri-quadratic interpolation of the displacement field. The tensor components in (6) are described with respect to a cylindrical coordinate system. This allows description of the LV wall with 1 circumferential element, thus reducing computational demand. In total, the LV wall is represented by 30 elements: 6 elements in radial, 1 in circumferential and 5 in longitudinal direction.

2.3. Simulations performed

Four simulations were performed with combinations of 2 initial conditions of $\alpha_{h,0}$ and 2 settings for the basal boundary conditions. Initial values of $\alpha_{h,0}$ were assumed to vary either nonlinearly (nLIN) or linearly (LIN) with the transmural position from endocardium to epicardium. The nonlinear distribution is obtained from Bovendeerd et al. (2009) (Fig. 3, dashed lines). The linear distribution varies from 60° at the endocardium to −60° at the epicardium (Fig. 4, dashed lines in simulations LIN). At the base, axial

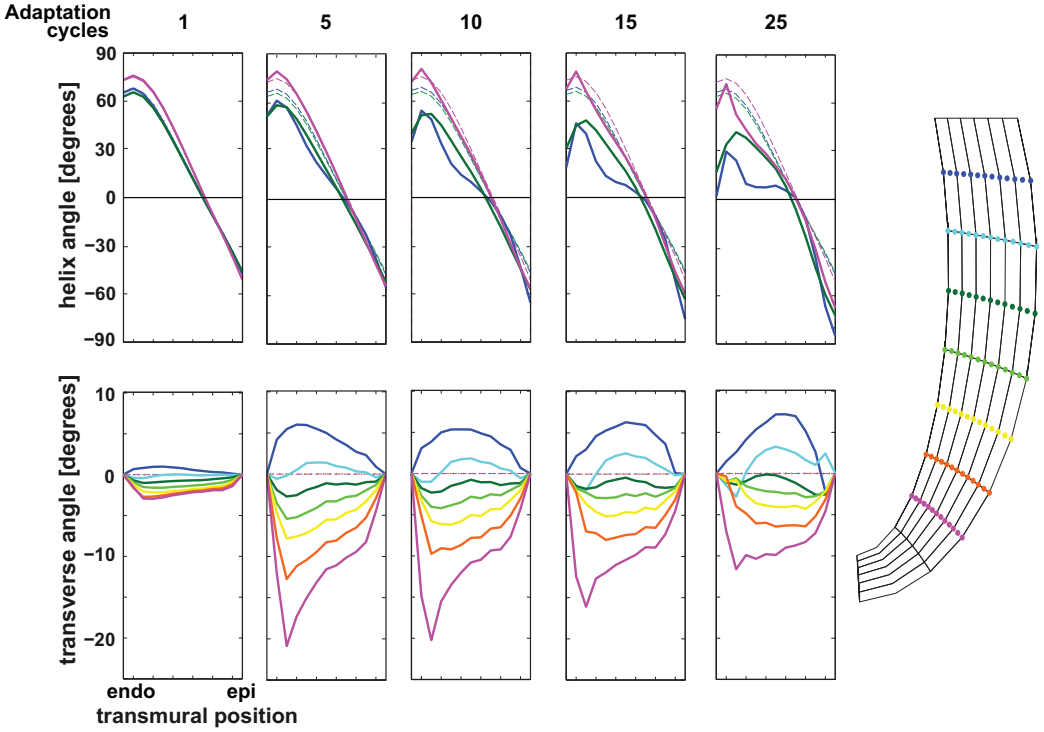

Fig. 3. Simulation FULL + nLIN. Development of helix angle $\alpha_{h,0}$ (top) and transverse angle $\alpha_{t,0}$ (bottom) after 1, 5, 10, 15, and 25 adaptation cycles. Transmural course in myofiber angles before (- -) and after (–) myofiber adaptation is shown for 7 longitudinal levels in the LV wall (right).

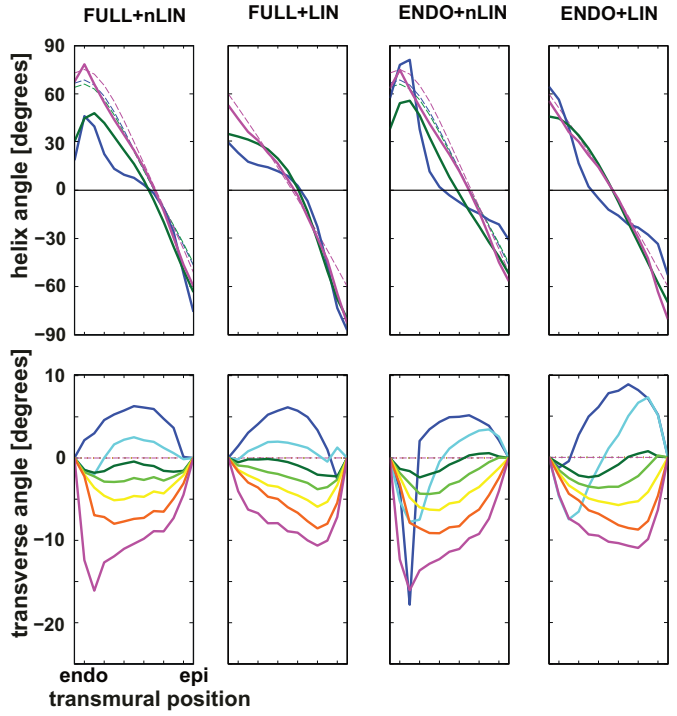

Fig. 4. Transmural course in helix angle $\alpha_{h,0}$ (top) and transverse angle $\alpha_{t,0}$ (bottom) in all simulations before adaptation (- -) and after 15 adaptation cycles (–) at the longitudinal levels shown in Fig. 3.

displacement was suppressed either at the whole basal surface (FULL), or at the endocardial ring only (ENDO). In both cases, circumferential displacement was only suppressed at the endocardial ring.

In all simulations, the first 10 consecutive cardiac cycles were used to reach a hemodynamic steady state and myofiber reorientation was not included. After these 10 cycles, myofiber reorientation was simulated over 25 adaptation cycles through the whole LV. Adaptation time constant κ was set to 3200 ms. Before reorientation, the transverse angle $\alpha_{t,0}$ in the reference state was set to zero.

2.4. Postprocessing

2.4.1. Quantification of adaptation process

Evolving fiber orientations, local mechanics, and global hemodynamics are analyzed to assess the effect of the adaptation process on LV structure and function. Baseline values are derived from the hemodynamic steady state after 10 cardiac cycles.

Structural response is quantified by changes in transmural distribution of angles $\alpha_{h,0}$ and $\alpha_{t,0}$ in 7 longitudinal levels from apex to base (Fig. 3, right). The angles are determined from the fiber vectors in a postprocessing step.

The effect of adaptation on local tissue mechanics is quantified by change in mean and standard deviation (SD) of five variables: maximum myofiber stress $\sigma_{f,max}$, stroke work density w_f, natural myofiber strain during isovolumic contraction $\epsilon_{f,ic}$, during ejection $\epsilon_{f,ej}$, and during isovolumic relaxation $\epsilon_{f,ir}$. The w_f at each point is defined as the area enclosed by the myofiber stress-natural strain loop:

$$w_f = \oint \sigma_f d\epsilon_f; \quad \epsilon_f = \ln \lambda_f \tag{7}$$

Evolution of homogeneity is quantified by the average of the SDs of strains $\epsilon_{f,ic}$, $\epsilon_{f,ej}$, and $\epsilon_{f,ir}$:

$$\overline{\mathrm{SD}}_{\epsilon_f} = \frac{\mathrm{SD}_{\epsilon_{f,ic}} + \mathrm{SD}_{\epsilon_{f,ej}} + \mathrm{SD}_{\epsilon_{f,ir}}}{3} \tag{8}$$

with $\mathrm{SD}_{\epsilon_{f,ic}}$, $\mathrm{SD}_{\epsilon_{f,ej}}$, $\mathrm{SD}_{\epsilon_{f,ir}}$, the SDs of $\epsilon_{f,ic}$, $\epsilon_{f,ej}$, and $\epsilon_{f,ir}$, respectively. Evolution of the SD of $\sigma_{f,max}$ (SD_σ) is analyzed too.

Global cardiac function is quantified by maximum LV pressure $p_{lv,max}$, stroke volume SV and stroke work W given by the area enclosed by the LV pressure–volume loop:

$$W = \oint p_{lv} dV_{lv} \tag{9}$$

2.4.2. Comparison with experimental data

Left ventricular circumferential–radial shear E_{cr} and torsion τ as computed with the model before and after myofiber reorientation are compared with those determined from magnetic resonance tagging (MRT) experiments. The protocol for the MRT measurements and determination of the Green–Lagrange strain tensor component E_{cr} have been described previously in Bovendeerd et al. (2009) and Ubbink et al. (2006). Definition of τ has been described previously in Delhaas et al. (2008). Essentially, τ quantifies the base-to-apex gradient of rotation about the LV long axis. E_{cr} quantifies the endo-to-epi gradient of this rotation. In the model, E_{cr} and τ are determined at the levels of the MR slices by interpolation from adjacent nodal points in the FE mesh. The locations of the MR slices relative to the model geometry are shown in Fig. 8 on the top left. In agreement with the experimental procedure, strains are computed with respect to begin-ejection and averaged in radial direction.

3. Results

Changes in transmural distribution of myofiber angles $\alpha_{h,0}$ and $\alpha_{t,0}$ in simulation FULL + nLIN are shown in Fig. 3. Within 1 adaptation cycle, a gradient for $\alpha_{t,0}$ develops with negative values at the apex and positive values at the base. Largest amplitudes develop within 5 adaptation cycles. Thereafter, the location of the extrema shifts from endocardium towards midwall. At the apical levels the amplitude decreases. As adaptation proceeds, endocardial $\alpha_{h,0}$ ($\alpha_{h,0}^{\mathrm{endo}}$) in the upper half of the LV wall evolves towards 0° (circumferentially oriented myofibers), whereas epicardial $\alpha_{h,0}$ ($\alpha_{h,0}^{\mathrm{epi}}$) evolves towards −90° (axially oriented myofibers).

In Fig. 4, transmural distributions of $\alpha_{h,0}$ and $\alpha_{t,0}$ are shown for all simulations after 15 adaptation cycles. The fast response of $\alpha_{t,0}$ and slow response of $\alpha_{h,0}$ were observed in the other simulations too. After 15 adaptation cycles, the effect of the initial condition of $\alpha_{h,0}$ (LIN vs. nLIN) was found to be reduced, while the effect of the basal boundary conditions (FULL vs. ENDO) persisted. As in FULL + nLIN, $\alpha_{h,0}^{\mathrm{endo}}$ evolves towards 0° and $\alpha_{h,0}^{\mathrm{epi}}$ towards −90° in FULL + LIN. For ENDO + nLIN and ENDO + LIN the opposite can be observed. In these simulations $\alpha_{h,0}^{\mathrm{endo}}$ evolves towards 90° (axial myofiber orientation) and $\alpha_{h,0}^{\mathrm{epi}}$ towards 0° (circumferential orientation). A similar gradient for $\alpha_{t,0}$ develops in all simulations. Near the base, $\alpha_{t,0}^{\mathrm{endo}}$ is positive for FULL + nLIN and FULL + LIN, whereas $\alpha_{t,0}^{\mathrm{endo}}$ is negative for ENDO + nLIN and ENDO + LIN.

In all simulations, local and global cardiac function increase significantly during the first adaptation cycles as indicated by the increase in maximum myofiber stress $\sigma_{f,max}$, stroke work density w_f, myofiber shortening (decrease of $\epsilon_{f,ej}$), maximum left ventricular pressure p_{lv}, stroke volume SV, and stroke work W. In addition, fiber strains during the isovolumic phases, $\epsilon_{f,ic}$ and $\epsilon_{f,ir}$, decrease significantly. Detailed results of simulation FULL + nLIN are shown

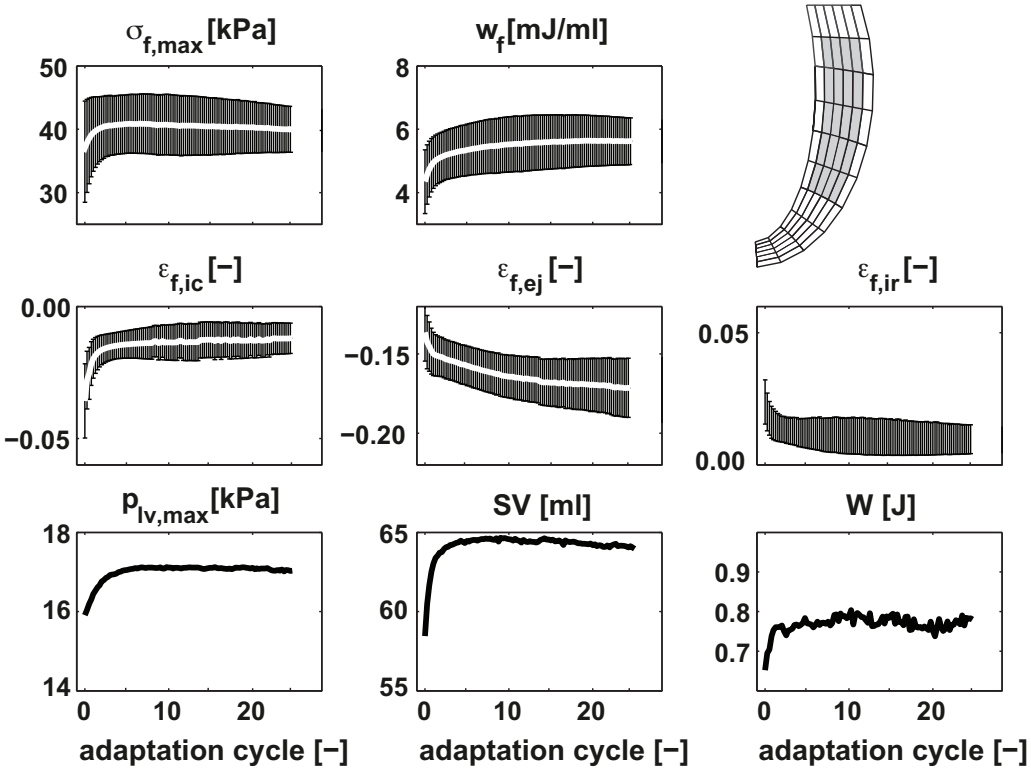

Fig. 5. Evolution of local and global function in FULL + nLIN during 25 adaptation cycles. Adaptation cycle is defined as time t normalized with respect to adaptation time constant κ (t/κ). Local function is presented by means and standard deviations calculated from the gray area indicated in the geometry (top right) of maximum myofiber stress $\sigma_{f,max}$, stroke work density w_f (top row), natural myofiber strain during isovolumic contraction $\epsilon_{f,ic}$, during ejection $\epsilon_{f,ej}$, and during isovolumic relaxation $\epsilon_{f,ir}$ (middle row). Global function is presented by maximum LV pressure $p_{lv,max}$, stroke volume SV, and stroke work W (bottom row).

in Fig. 5. For all simulations, evolution of homogeneity is indicated in Fig. 6 where development of $\overline{\mathrm{SD}}_{\epsilon_f}$ and SD_σ are shown. Here, a fast response during the first adaptation cycles is observed too. All simulations show an increase in homogeneity of average strain during the first adaptation cycles. Strain homogeneity increases further in simulations LIN, while it decreases in simulations nLIN. During the whole adaptation process, homogeneity of $\sigma_{f,max}$ increases for all simulations except for ENDO + nLIN. In ENDO + nLIN, both $\overline{\mathrm{SD}}_{\epsilon_f}$ and SD_σ reach a minimum after 2 adaptation cycles. Finally, $\overline{\mathrm{SD}}_{\epsilon_f}$ and SD_σ evolve to 2 values, solely dependent on the basal boundary conditions.

For all simulations, the model predicts fiber structures with distributions of $\alpha_{h,0}$ and $\alpha_{t,0}$ within the, admittedly wide, range of experimental data (Fig. 7). Furthermore, patterns of circumferential–radial shear E_{cr} are more realistic after myofiber reorientation (Fig. 8). E_{cr} amplitudes reduce from ~0.35 before to ~0.18 after reorientation, while experimental amplitudes of ~0.1 are observed. Before adaptation, the axial gradient of E_{cr} at end-ejection is opposite to experimental observations. After adaptation, the gradient flips and becomes similar to the experiment. Before adaptation, two characteristic patterns of torsion τ can be observed, determined by the initial conditions of $\alpha_{h,0}$ (LIN vs. nLIN). Differences in τ disappear after adaptation. Minimum τ is reached before end of ejection, which is early when compared with experimental τ. The return to zero of τ occurs slower in the model than in the experiment.

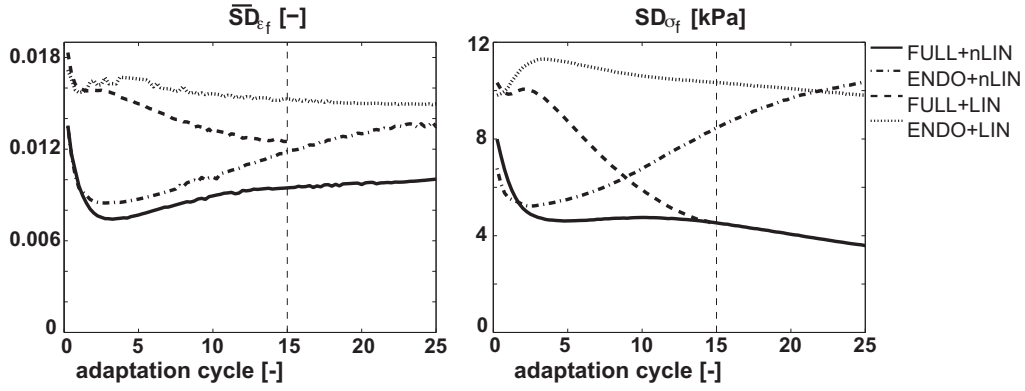

Fig. 6. Evolution of average standard deviation (SD) of strains ($\overline{\mathrm{SD}}_{\epsilon_f}$, left) and SD of maximum myofiber stress $\sigma_{f,max}$ (SD_{σ_f}, right) in simulations FULL + nLIN (–), ENDO + nLIN (-·-·), FULL + LIN (- - -), and ENDO + LIN (· · ·). Adaptation cycle is defined as time t normalized with respect to adaptation time constant κ (t/κ). The verticle dashed line indicates the moment in time at which results in Fig. 4 are presented.

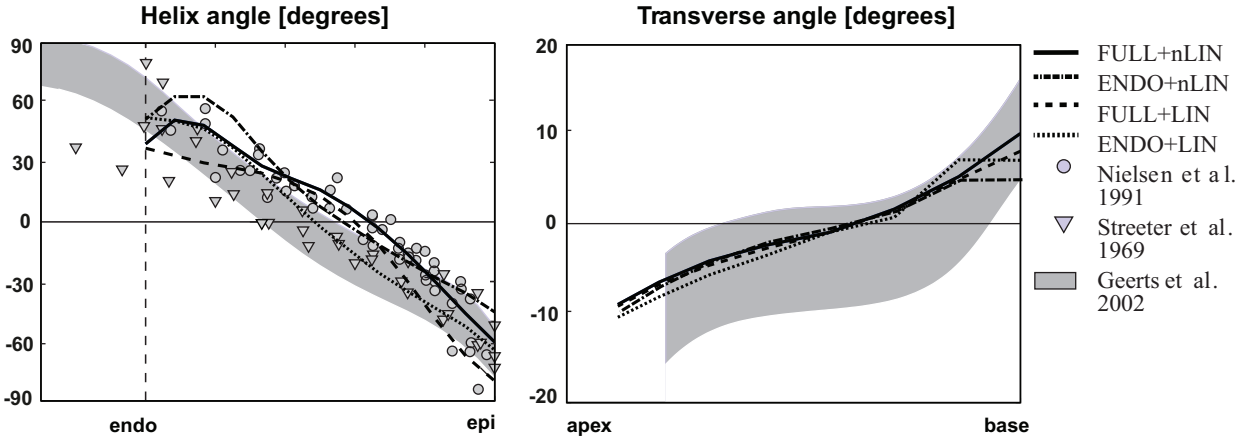

Fig. 7. Comparison of predicted myocardial structure after 15 adaptation cycles with experimental data (Geerts-Ossevoort et al., 2002; Nielsen et al., 1991; Streeter et al., 1969). Left: Helix angle $\alpha_{h,0}$ at equatorial level. Right: Transverse angle $\alpha_{t,0}$ at mid-wall. The mid-wall region was defined as the transmural region with an absolute helix angle value of less than 5°.

4. Discussion

In this study, we further investigated a computational model in which left ventricular (LV) myofiber reorientation was considered as a local response to local fiber cross-fiber shear strain (Kroon et al., 2009a). The effect of the initial fiber orientations, and the influence of the boundary conditions at the base on the long-term outcome of the adaptive process were investigated.

In all simulations, a fast development of transverse angle $\alpha_{t,0}$ and a slow response of helix angle $\alpha_{h,0}$ were observed. This is

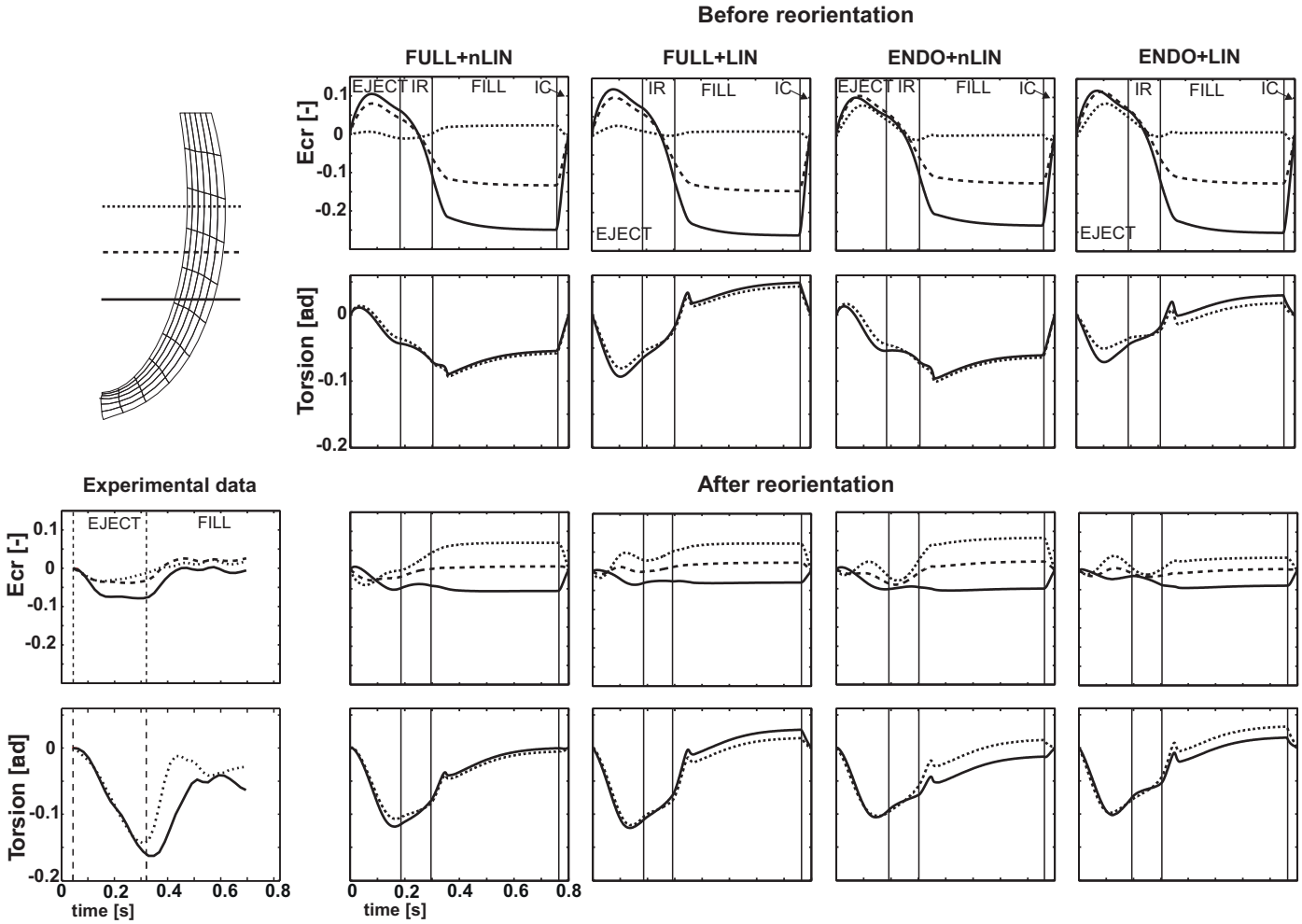

Fig. 8. Model computed circumferential–radial shear E_{cr} in 3 short axis slices and torsion τ in between these slices before adaptation (top) and after 15 adaptation cycles (bottom). On the top left, the LV geometry in simulation FULL + nLIN at begin ejection is shown with the position of the 3 short axis slices relative to the geometry. On the bottom left, a typical example of experimental data is presented (Bovendeerd et al., 2009). EJECT, ejection phase; IR, isovolumic relaxation phase; FILL, filling phase; IC, isovolumic contraction phase.

presumably caused by the fact that the initial $\alpha_{h,0}$ was chosen in the range of experimental data, while $\alpha_{t,0}$ was set to an unphysiological value of zero. From the transmural distributions of fiber angles (Fig. 4) and from the evolution of homogeneity in stress and strain (Fig. 6), it was observed that the simulations with the same boundary condition showed a similar behavior during adaptation that was irrespective of the initial fiber orientation. The effect of the initial condition of $\alpha_{h,0}$ on especially homogeneity diminishes during adaptation: simulations where boundary conditions were applied at the whole basal surface (FULL) evolved to similar SD values (Fig. 6). So did the simulations where boundary conditions were applied at the endocardial basal ring (ENDO). This suggests that one single optimal fiber orientation exists, which agrees with observations in optimization studies (Rijcken et al., 1999; Vendelin et al., 2002).

The basal boundary conditions had a significant effect on the adaptation process. Initially, the basal boundary conditions affect deformation near the base only. This deformation pattern affects fiber reorientation in the basal region, which in turn affects deformation also in regions closer to the equator. Thus, basal boundary conditions gradually affect fiber orientation in the complete LV (Fig. 3).

To enforce boundary conditions, external forces are implicitly applied. Fibers near the base tend to align in the direction of these forces. Consequently, in simulations FULL, fibers oriented perpendicular to the epicardial base ($\alpha_{h,0}$ towards -90°), whereas in simulations ENDO, they oriented towards the endocardial basal ring only (negative $\alpha_{t,0}$, $\alpha_{h,0}$ towards 90°, Fig. 4). The latter pattern is more in agreement with anatomical data. However, considering the amplitude of radial–axial shear strain E_{rz} near the base, values in simulations FULL ($\sim$0.08) are closer to experimental values ($\sim$0.02, Young et al., 1994) than those in simulations ENDO ($\sim$0.20), suggesting that the boundary conditions in simulations FULL are more realistic. Prescribing boundary conditions in terms of forces instead of displacements, i.e., allowing limited axial basal movement, might be a more realistic way for modeling boundary conditions at the base (Saint-Marie et al., 2006).

A decrease of myofiber strain during the isovolumic phases ($\epsilon_{f,ic}$ and $\epsilon_{f,ir}$) was observed in all simulations and indicated that differences between fiber orientations in the loaded and unloaded tissue indeed decreased. Thus, fiber cross-fiber shear minimized as a result of deformation-induced reorientation. Fiber directions evolved towards a principal strain direction that was not prescribed in Eq. (1). At begin ejection, we found that the minimal stretch direction was oriented perpendicular to the LV wall. Consequently, intermediate and maximum stretch directions are oriented within the plane of the wall. It turned out that fiber directions evolved towards the intermediate stretch direction, in agreement with the expectation that active fibers generate a compressive force on the tissue along their direction.

4.1. Comparison with experimental data

From the comparison with experimental data (Fig. 7), no model can be preferred since predicted values of $\alpha_{h,0}$ and mid-wall $\alpha_{t,0}$ were quite similar for all simulations. However, restriction to presentation of mid-wall $\alpha_{t,0}$ neglects the transmural differences which were clearly visible in Fig. 4. Since no experimental data on the transmural variation of the transverse angle exists, the model could not be verified in this respect.

The transmural distribution of the transverse angle is important since it determines the pattern of circumferential–radial shear E_{cr} (Bovendeerd et al., 2009). E_{cr} patterns were more realistic after myofiber reorientation in all simulations (Fig. 8). The improved agreement between E_{cr} in simulation FULL + nLIN and experiment was previously presented by Kroon et al. (2009b), and is in line with the study by Bovendeerd et al. (2009), where it was concluded that agreement with experimental data could only be obtained when a non-zero $\alpha_{t,0}$ was included. Ubbink et al. (2006) demonstrated a high sensitivity of E_{cr} on $\alpha_{t,0}$. Differences in transmural variation of $\alpha_{t,0}$ might therefore explain the differences in E_{cr} patterns between simulations.

Before reorientation, two torsion patterns can be distinguished (Fig. 8). Since $\alpha_{t,0}$ was set to zero in all simulations, the differences might be a result of the differences in $\alpha_{h,0}$. After reorientation, τ-patterns were similar, despite differences in $\alpha_{h,0}$ and $\alpha_{t,0}$. The early appearance of the minimum in τ and the slow return to zero as compared to experiments, presumably were a result of the choice of the time constants for onset and decay of active stress. Furthermore, the 'hump' in the τ-pattern early in the filling phase, was found to be the result of inhomogeneous relaxation. In the model, sarcomere length was assumed homogeneous in the unloaded LV. As a result, sarcomere length is inhomogeneous at begin contraction. Since both the level of actively generated myofiber stress and the duration of the twitch are directly related to sarcomere length, relaxation is inhomogeneous. In a simulation where sarcomere length was chosen homogeneous at begin contraction, relaxation was homogeneous and the 'hump' disappeared.

4.2. Study assumptions and model limitations

The model presented only accounts for myofiber reorientation. Other adaptation mechanisms are likely to be active as well. Clinically, one of the most evident examples of adaptation is the change in LV wall mass and cavity volume in response to pressure and volume overload, respectively. In addition, in reality the externally unloaded LV exhibits a transmural gradient in sarcomere length with epicardial sarcomeres being longer than endocardial ones (Rodriguez et al., 1993). This might be a result of mechanically induced adaptation as well. Extension of the model with these adaptive mechanisms should be considered.

5. Conclusions

In this study, we further investigated a computational model of shear-induced myofiber reorientation in the left ventricular wall. It is concluded that the choice of boundary conditions at the base influences long-term development of fiber orientation while the effect of initial setting of fiber orientation field disappears. Thus, for modeling adaptive reorientation of myofibers, physiological boundary conditions at the base are relevant. Due to large spread in experimental data on fiber orientation and the lack of detailed data on the transverse angle at the base, no clear conclusion can be drawn with respect to which of the boundary conditions is preferable. After reorientation, differences between model predicted and experimental observation of LV structure and deformation were reduced significantly, but a complete match could not be obtained.

References

Arts, T., Prinzen, F.W., Snoeckx, L.H., Rijcken, J.M., Reneman, R.S., 1994. Adaptation of cardiac structure by mechanical feedback in the environment of the cell: a model study. Biophys. J. 66, 953–961.

Bovendeerd, P.H.M., Kroon, W., Delhaas, T., 2009. Determinants of left ventricular shear strain. Am. J. Physiol. Heart Circ. Physiol. 297, H1058–H1068.

Costa, K.D., Holmes, J.W., McCulloch, A.D., 2001. Modelling cardiac mechanical properties in three dimensions. Phil. Trans. R. Soc. Lond. A 359, 1233–1250.

Delhaas, T., Arts, T., Bovendeerd, P.H.M., Prinzen, F.W., Reneman, R.S., 1993. Subepicardial fiber strain and stress as related to left ventricular pressure and volume. Am. J. Physiol. Heart Circ. Physiol. 264, H1548–H1559.

Delhaas, T., Kroon, W., Decaluwe, W., Rubbens, M.P., Bovendeerd, P.H.M., Arts, T., 2008. Structure and torsion of the normal and situs inversus totalis cardiac left ventricle. Part I: experimental data in humans. Am. J. Physiol. Heart Circ. Physiol. 295, H197–H201.

Geerts-Ossevoort, L., Bovendeerd, P.H.M., Nicolay, N., Arts, T., 2002. Characterization of the normal cardiac myofiber field in goat measured with MR-diffusion tensor imaging. Am. J. Physiol. Heart Circ. Physiol. 283, H139–H145.

Hunter, P.J., Coveney, P.V., De Bono, B., Diaz, V., Fenner, J., Frangi, A.F., Harris, P., Hose, R., Kohl, P., Lawford, P., McCormack, K., Mendes, M., Omholt, S., Quarteroni, A., Skår, J., Tegner, J., Thomas, S.R., Tollis, I., Tsamardinos, I., Van Beek, J.H.G.M., Viceconti, M., 2010. A vision and strategy for the virtual physiological human in 2010 and beyond. Phil. Trans. R. Soc. Lond. A 368, 2595–2614.

Kerckhoffs, R.C.P., Bovendeerd, P.H.M., Kotte, J.C.S., Prinzen, F.W., Smits, K., Arts, T., 2003. Homogeneity of cardiac contraction despite physiological asynchrony of depolarization: a model study. Ann. Biomed. Eng. 31, 536–547.

Kroon, W., Delhaas, T., Arts, T., Bovendeerd, P.H.M., 2009a. Computational analysis of the myocardial structure: adaptation of myofiber orientations through deformation in three dimensions. Med. Image Anal. 13, 346–353.

Kroon, W., Delhaas, T., Bovendeerd, P.H.M., Arts, T., 2009b. Adaptive reorientation of cardiac myofibers: comparison of left ventricular shear in model and experiment. In: Ayache, N., et al. (Eds.), Funct. Imaging Model. Heart. Springer Verlag Berlin/Heidelberg, pp. 58–67, ISBN-13: 978-3-642-01931-9.

Nielsen, P.M., LeGrice, I.J., Smaill, B.H., Hunter, P.J., 1991. Mathematical model of geometry and fibrous structure of the heart. Am. J. Physiol. Heart Circ. Physiol. 260, H1365–H1378.

Rijcken, J.M., Bovendeerd, P.H.M., Schoofs, A.J.G., Van Campen, D.H., Arts, T., 1999. Optimization of cardiac fiber orientation for homogeneous fiber strain during ejection. Ann. Biomed. Eng. 27, 289–297.

Rodriguez, E.K., Omens, J.H., Waldman, L.K., McCulloch, A.D., 1993. Effect of residual stress on transmural sarcomere length distributions in rat left ventricle. Am. J. Physiol. Heart Circ. Physiol. 264, H1048–H1056.

Saint-Marie, J., Chapelle, D., Cimrman, R., Sorine, M., 2006. Modeling and estimation of the cardiac electromechanical activity. Comput. Struct 84, 1743–1759.

Streeter Jr., D.D., Spotnitz, H.M., Platel, D.J., Ross Jr., J., Sonnenblick, E.H., 1969. Fiber orientation in the canine left ventricle during diastole and systole. Circ. Res. 24, 339–347.

Ubbink, S.W.J., Bovendeerd, P.H.M., Delhaas, T., Arts, T., Van de Vosse, F.N., 2006. Towards model-based analysis of cardiac MR tagging data: relation between left ventricular shear strain and myofiber orientation. Med. Image Anal. 10, 623–641.

Vendelin, M., Bovendeerd, P.H.M., Engelbrecht, J., Arts, T., 2002. Optimizing ventricular fibers: uniform strain of stress, but not ATP consumption, leads to high efficiency. Am. J. Physiol. Heart Circ. Physiol. 283, H1072–H1081.

Waldman, L.K., Nosan, D., Villarreal, F., Covell, J.W., 1988. Relation between transmural deformation and local myofiber direction in canine left ventricle. Circ. Res. 63, 550–562.

Weis, S.M., Emery, J.L., Becker, K.D., McBride Jr., D.J., Omens, J.H., McCulloch, A.D., 2000. Myocardial mechanics and collagen structure in the osteogenesis imperfecta murine (oim). Circ. Res. 87, 663–669.

Young, A., Kramer, C., Ferrari, V., Axel, L., Reichek, N., 1994. Three-dimensional left ventricular deformation in hypertrophic cardiomyopathy. Circulation 90, 854–867.

Zimmerman, S.D., Karlon, W.J., Holmes, J.W., Omens, J.H., Covell, J.W., 2000. Structural and mechanical factors influencing infarct scar collagen organization. Am. J. Physiol. Heart Circ. Physiol. 278, H194–H200.